

# PCCP

Accepted Manuscript



This is an *Accepted Manuscript*, which has been through the Royal Society of Chemistry peer review process and has been accepted for publication.

*Accepted Manuscripts* are published online shortly after acceptance, before technical editing, formatting and proof reading. Using this free service, authors can make their results available to the community, in citable form, before we publish the edited article. We will replace this *Accepted Manuscript* with the edited and formatted *Advance Article* as soon as it is available.

You can find more information about *Accepted Manuscripts* in the [Information for Authors](#).

Please note that technical editing may introduce minor changes to the text and/or graphics, which may alter content. The journal's standard [Terms & Conditions](#) and the [Ethical guidelines](#) still apply. In no event shall the Royal Society of Chemistry be held responsible for any errors or omissions in this *Accepted Manuscript* or any consequences arising from the use of any information it contains.



## Physical Chemistry Chemical Physics

## PAPER

Defect chemistry and lithium transport in Li<sub>3</sub>OCl anti-perovskite superionic conductor

Received 00th January 20xx,  
Accepted 00th January 20xx

DOI: 10.1039/x0xx00000x

www.rsc.org/

Ziheng Lu,<sup>a,b</sup> Chi Chen,<sup>a</sup> Zarah Medina Baiyee,<sup>a</sup> Xin Chen,<sup>b</sup> Chunming Niu<sup>b</sup> and Francesco Ciucci<sup>a, c, \*</sup>

Lithium-rich anti-perovskites (LiRAPs) are a promising family of solid electrolytes, which exhibit ionic conductivities above  $10^{-3}$  S/cm at room temperature, among the highest reported to date. In this work, we investigate the defect chemistry and associated lithium transport in Li<sub>3</sub>OCl, a prototypical LiRAP, by *ab initio* density functional theory (DFT) calculations and classical molecular dynamics (MD) simulations. We studied three types of charge neutral defects, namely the LiCl Schottky pair, the Li<sub>2</sub>O Schottky pair, and the Li interstitial with a substitutional defect of O on Cl site. Among them the LiCl Schottky pair has the lowest binding energy and is most energetically favorable for diffusion as computed by DFT. This is confirmed by classical MD simulations where the computed Li ion diffusion coefficients in LiCl Schottky systems are significantly higher than those for the other two defects considered and the activation energy in LiCl deficient Li<sub>3</sub>OCl is comparable to experimental values. The high conductivities and low activation energies of LiCl Schottky systems are explained by the low energy pathways of Li between the Cl vacancies. We propose that Li vacancy hopping is the main diffusion mechanism in highly conductive Li<sub>3</sub>OCl.

## 1. Introduction

Lithium ion batteries (LIBs) have received increasing attention during the past decades due to their high energy density and low self-discharge rate and have become the dominant power source for portable electronics.<sup>1-5</sup> However, LIBs today still suffer from safety issues, including the flammability of typical organic liquid electrolytes.<sup>6,7</sup> This is a particularly serious concern for electrical vehicles. Generally, replacing liquid electrolytes with inorganic solid electrolytes may solve this problem. However, the ionic conductivities of most solid electrolytes are several orders of magnitude lower than those of liquid electrolytes, limiting their practical use.<sup>8</sup>

During the past few years, several types of solid electrolyte materials with high ionic conductivities have been synthesized, including NASICON-type (sodium super ionic conductors) phosphates,<sup>9,10</sup> garnet-type Li<sub>7</sub>La<sub>3</sub>Zr<sub>2</sub>O<sub>12</sub> (LLZO),<sup>11,12</sup> glass-ceramic-type-lithium sulphide,<sup>13,14</sup> anti-perovskite-type Li<sub>3</sub>OA,<sup>15</sup> and Li<sub>10</sub>GeP<sub>2</sub>S<sub>12</sub>.<sup>16</sup> Among these emerging materials, the anti-perovskite Li<sub>3</sub>OA (A = halogen) family first developed by Zhao *et al.*<sup>15</sup> is attracting increasing attention due to its high ionic conductivity (above  $10^{-3}$  S/cm at room temperature and  $10^{-2}$  S/cm below melting temperature), low activation enthalpy,

negligible electronic conductivity, wide electrochemical window (>5 V), good cyclability, light weight, and low costs of the raw materials used in the synthesis.<sup>15</sup>

The Li<sub>3</sub>OA lithium conductors are characterized by an anti-perovskite crystal structure which bears some resemblance to that of typical ABO<sub>3</sub> perovskite oxides. While in conventional perovskite, A and B sites are occupied by cations, in lithium rich anti-perovskites (LiRAPs), the A counterpart is occupied by a negatively charged halogen, the site corresponding to B by O<sup>2-</sup>, and the oxygen counter part by Li<sup>+</sup>. The configuration of Li<sub>3</sub>OCl, a typical LiRAP, is shown for reference in Fig. 1. The Li, Cl and O atoms are located at the octahedral vertices, octahedral centers and cube centers, respectively. It is suggested that by deliberately mixing A site halogens, doping lithium sites with divalent metals and depleting LiA units, Li<sub>3-x-δ</sub>M<sub>x/2</sub>O(A<sub>1-y</sub>A'<sub>y</sub>)<sub>1-δ</sub> could be obtained so as to increase the conductivity.<sup>15</sup> Recently, Braga *et al.*<sup>17</sup> developed a series of Li-rich anti-perovskite derivatives, namely Li<sub>3-2x</sub>M<sub>x</sub>AO glasses (M = divalent metal, A = halogen), based on divalent metal doped Li<sub>3</sub>OCl. These LiRAP based glasses have the highest reported ionic conductivity among all known solid lithium ionic conductors ( $2.5 \times 10^{-2}$  S/cm at room temperature).

<sup>a</sup> Department of Mechanical and Aerospace Engineering, The Hong Kong University of Science and Technology, Hong Kong, China

<sup>b</sup> Center of Nanomaterials for Renewable Energy, State Key Laboratory of Electrical Insulation and Power Equipment, School of Electrical Engineering, Xi'an Jiaotong University, Xi'an 710049, China

<sup>c</sup> Department of Chemical and Biomolecular Engineering, The Hong Kong University of Science and Technology, Hong Kong, China

E-mail: francesco.ciucci@ust.hk; Tel: +852 2358 7187

† Electronic Supplementary Information (ESI) available. DOI: 10.1039/x0xx00000x

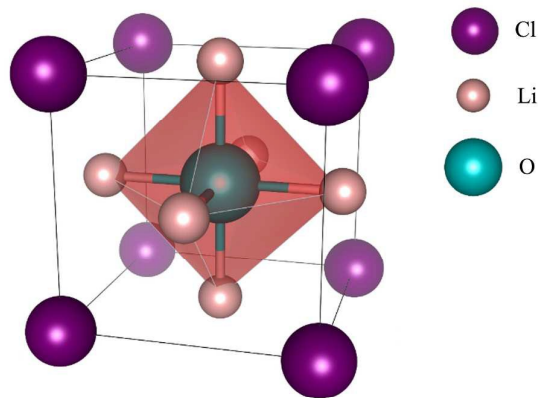


Fig. 1 Atomic structure of  $\text{Li}_3\text{OCl}$  in a unit cell. Lithium, oxygen and chlorine atoms are located at the octahedral vertices, octahedral centers and cube vertices respectively.

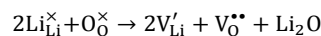
In spite of the superb properties of Li-rich anti-perovskites, the conductivity mechanism is still not well understood. Several theoretical works have focused on the phase stability<sup>18–20</sup> Li migration mechanism,<sup>18,19,21</sup> charge carrier concentration<sup>21</sup> and compositional optimization<sup>22</sup> by first principle calculations and lattice dynamics calculations. Zhang *et al.*<sup>18</sup> and Mouta *et al.*<sup>21</sup> reported a high formation energy  $>1.5$  eV for a lithium Frenkel pair. This finding rules out the possibility that the main mechanism of Li transport involves the formation and recombination of lithium vacancy and interstitial pairs. Zhang *et al.*<sup>18</sup> proposed the lithium vacancy hopping mechanism and calculated the migration barrier to be 367 meV. Deng *et al.*,<sup>22</sup> further identified a lower barrier of Li vacancy (282 meV) by varying the halide sublattice ordering. In contrast, Emly *et al.*<sup>19</sup> proposed a migration mechanism involving Li interstitial dumbbells with a computed energy barrier 50% lower than that of the vacancy-driven migration. To date, there seems to be no consensus on the mechanism of Li transport in  $\text{Li}_3\text{OCl}$ .

In this work we study the defect chemistry and Li transport in  $\text{Li}_3\text{OCl}$  and aim at bridging this gap in the literature. We note that in order to ensure charge neutrality, the charge transport intermediates, i.e., lithium vacancies (Kröger–Vink notation  $V_{\text{Li}}^{\times}$ 's) or lithium interstitials ( $\text{Li}_i^{\bullet}$ 's) need to exist in pair with counter charge defects. For example,  $V_{\text{Li}}^{\times}$ 's pair with  $V_{\text{Cl}}^{\bullet}$ 's or  $V_{\text{O}}^{\bullet}$ 's and  $\text{Li}_i^{\bullet}$ 's pair with  $\text{O}_{\text{Cl}}^{\times}$ 's. We considered in this article these three types of charge neutral defect pairs, namely the LiCl Schottky pair,  $\text{Li}_2\text{O}$  Schottky pair, and Li interstitial with a substitutional defect of O on a Cl site. In fact their formation energies have been reported to be relatively low.<sup>19</sup> Additionally, the formation of such charge neutral defect pairs leads to non-stoichiometric systems ( $\text{Li}_{3-x}\text{OCl}_{1-x}$ ,  $\text{Li}_{3-x}\text{O}_{1-0.5x}\text{Cl}$  and  $\text{Li}_{3+x}\text{O}_{1+x}\text{Cl}_{1-x}$ ) and has been suggested in both experimental and theoretical works.<sup>15,19,21</sup> The corresponding defect reactions are listed:

(a) LiCl Schottky pair ( $V_{\text{Li}}^{\times}-V_{\text{Cl}}^{\bullet}$ ):



(b)  $\text{Li}_2\text{O}$  Schottky pair ( $2V_{\text{Li}}^{\times}-V_{\text{O}}^{\bullet}$ ):



(c)  $\text{Li}_2\text{O}$  solution ( $\text{Li}_i^{\bullet}-\text{O}_{\text{Cl}}^{\times}$ ):



We computed formation energies, configurations and binding energies for the three types of defects using DFT. Their diffusional properties were assessed using classical MD simulations. We found that among the investigated systems, the ionic conductivities of LiCl deficient LiRAPs are the highest. This is due to the comparatively weak defect attraction between  $V_{\text{Li}}^{\times}$  and  $V_{\text{Cl}}^{\bullet}$ . More significantly, the low activation energies computed based on MD simulations agree well with experimental results.<sup>15</sup> Therefore, we propose that Li vacancy hopping is the main diffusion mechanism in highly conductive  $\text{Li}_3\text{OCl}$ . The results provide not only an atomistic mechanism for Li transport in LiRAPs, but also some guidance to experimentalists in the synthesis of high conductivity LiRAPs.

## 2. Methodology

### 2.1 Density functional theory

All DFT calculations were carried out using VASP<sup>23</sup> with the Perdew–Burke–Ernzerhof generalized gradient approximation. The structural relaxation for defect configurations and the calculation of binding energies were performed on a  $3 \times 3 \times 3$  supercells containing 135 atoms (for defect free systems). The projector augmented wave (PAW) method<sup>24</sup> with a plane-wave basis set was used. The Brillouin zone was sampled by  $3 \times 3 \times 3$  Monkhorst–Pack grid. For oxygen, chlorine, and lithium, we used pseudopotentials with valence configuration  $2s^2 2p^4$ ,  $3s^2 3p^5$ , and  $1s^2 2s^1$ . The energy cutoff was set to 600 eV. The partial occupancies of electrons were determined using Gaussian smearing with a 0.05 eV window. The convergence criterion of the electron self-consistent loop was set to be  $10^{-5}$  eV. The supercell box size was initialized at  $11.71 \text{ \AA} \times 11.71 \text{ \AA} \times 11.71 \text{ \AA}$ . All energies were minimized using the conjugate gradient algorithm until the Hellman–Feynman forces acting on each atom were smaller than  $10^{-6} \text{ eV/\AA}$ . In order to identify the minimum energy defect configurations, the  $V_{\text{Li}}^{\times}$ 's (or  $\text{Li}_i^{\bullet}$ 's) were initialized at different places with respect to  $V_{\text{Cl}}^{\bullet}/V_{\text{O}}^{\bullet}$  ( $\text{O}_{\text{Cl}}^{\times}$ ) and then relaxations were performed. The energy of the most stable defect configuration (arrangement of defect pairs) is noted as  $E_{\text{min}}$ . Other configurations all have higher energies, which are noted as  $E$  (local energy minima). The energy difference (relative energy)  $\Delta E$  between these configurations and the most stable one was calculated using

$$\Delta E = E - E_{\text{min}} \quad (1)$$

The binding energy of a defect pair was calculated using a supercell approach following the work by Nakayama *et al.*<sup>25</sup>

$$E_{\text{binding}} = \sum E_{\text{isolated defect}} - E_{\text{cluster}} \quad (2)$$

where  $E_{\text{binding}}$ ,  $E_{\text{cluster}}$ , and  $E_{\text{isolated defect}}$  are the binding energy of a defect pair, the formation energy of a defect pair, and the formation energies of separated defects respectively.

**Table 1** Buckingham potential parameters<sup>21</sup>

Interaction	$A_{\alpha\beta}$ /eV	$\rho_{\alpha\beta}$ /Å	$C_{\alpha\beta}$ /eVÅ <sup>6</sup>
O <sup>2-</sup> -O <sup>2-</sup>	22764.3000	0.1490	13.1850
Cl <sup>-</sup> -Cl <sup>-</sup>	5145.2755	0.3066	20.5230
Li <sup>+</sup> -O <sup>2-</sup>	433.2627	0.3138	0
Li <sup>+</sup> -Cl <sup>-</sup>	421.0366	0.3364	0
Li <sup>+</sup> -Li <sup>+</sup>	360.5269	0.1609	0

In order to increase clarity, the calculation of the binding energy of a LiCl Schottky pair is detailed in Section 2 of the Supplementary Information.

## 2.2 MD simulations

Classical MD simulations were carried out using LAMMPS<sup>26</sup> with a time step of 1 fs. All ions were assumed to be fully charged and only pairwise interactions were considered. The ionic pair interactions were simulated via the Buckingham potential model, which takes the following analytic form:

$$\Phi_{\alpha\beta(\alpha\neq\beta)} = \frac{z_{\alpha} z_{\beta}}{4\pi\epsilon r_{\alpha\beta}} + A_{\alpha\beta} \exp\left(-\frac{r_{\alpha\beta}}{\rho_{\alpha\beta}}\right) - \frac{C_{\alpha\beta}}{r_{\alpha\beta}^6} \quad (3)$$

where  $z_{\alpha}$  and  $z_{\beta}$  are the charge numbers of the two interacting ions  $\alpha$  and  $\beta$ ,  $\epsilon$  is the dielectric constant, and  $r_{\alpha\beta}$  is the distance between the two ions. The potential parameters,  $A_{\alpha\beta}$ ,  $\rho_{\alpha\beta}$ , and  $C_{\alpha\beta}$ , were taken from previously published work by Mouta *et al.*<sup>21</sup> and are reported in **Table 1**. In all simulations, we used 10×10×10 supercells containing ~5000 atoms (exactly 5000 atoms for defect free system) with defect concentrations of  $x=0.01, 0.02, 0.05, 0.10$  and  $0.15$ . The systems were first equilibrated in the NPT ensemble for 200 ps followed by a 2 ns NVT run. We used the NVT trajectories to calculate the diffusion coefficients from corresponding mean squared displacements. We obtained the conductivities from self-diffusivities using the Nernst-Einstein relation, assuming that all Li ion hopping events are independent.<sup>27</sup>

We also carried out force-field based nudged elastic band (FF-NEB) calculations to benchmark upon the published DFT-NEB results<sup>18</sup> in a 3×3×3 charged supercell with a force convergence of 10<sup>-5</sup> eV/Å and an energy convergence of 10<sup>-6</sup> eV/atom. 13 images were used in this calculation.

## 3. Results and Discussion

### 3.1 Defect formation, dissociation and migration with DFT

**Defect formation.** We first calculated the formation energies of defects using DFT. The charge neutral defects considered here are listed in (a)-(c) as shown in Section 1. We also computed formation energy for the Li Frenkel pair, i.e.  $\text{Li}_i^+ - \text{V}_{\text{Li}}'$ , so as to make our work complete.

As shown in **Table 2**, lithium Frenkel pairs ( $\text{Li}_i^+ - \text{V}_{\text{Li}}'$ ) have a high formation energy of ~2 eV. The computed value is in agreement with the results of Emly *et al.*<sup>19</sup> This large value implies that it is difficult to form lithium Frenkel pairs. Therefore, the concentration might be low at the working temperature of Li<sub>3</sub>OCl. This is also supported by the MD

**Table 2** Defect formation energies of a LiCl Schottky pair, a Li<sub>2</sub>O Schottky pair, a Li interstitial, and a Li Frenkel pair.

Defect pair	$V_{\text{Li}}' - V_{\text{Cl}}'$	$2V_{\text{Li}}' - V_{\text{O}}^{**}$	$\text{Li}_i^+ - \text{O}_{\text{Cl}}'$	$\text{Li}_i^+ - \text{V}_{\text{Li}}'$
Defect reaction*	(a)	(b)	(c)	-
Formation energy/eV	1.41	1.60(0.8/ $V_{\text{Li}}'$ )	1.67	2.02
Reference	0.93 <sup>21</sup>	1.56 <sup>21</sup>	N/A	1.96 <sup>19</sup>

\* The defect reactions correspond to the ones shown in Section 1

simulations of defect-free systems where no effective Li ion hopping events were observed in perfect lattice as shown in **Fig. S3**. Thus, lithium Frenkel pairs are not discussed further in this article. The formation energies of the LiCl Schottky ( $V_{\text{Cl}}' - V_{\text{Li}}'$ ), Li<sub>2</sub>O Schottky ( $2V_{\text{Li}}' - V_{\text{O}}^{**}$ ) and Li interstitial with a substitutional O on Cl site ( $\text{Li}_i^+ - \text{O}_{\text{Cl}}'$ ) are 1.41 eV, 1.60 eV, and 1.67 eV, respectively.

These values are comparatively lower than the Li Frenkel pair formation energy supporting the argument that the non-stoichiometric compounds are formed at high temperatures. However, various authors reported that the synthesis method do not allow the control of the concentration of defects.<sup>15,21</sup> Thus it is difficult to precisely calculate the absolute values of defect concentrations. Here, based on the defect formation energies from DFT calculations, we only established a rough order of formation probability. That is, while the three types of defect pairs have comparable formation energies, it is slightly easier to form LiCl Schottky pairs.

**Defect configurations.** The calculations of above mentioned formation energies are based on the lowest energy configurations where the two defects in a defect pair are located near each other. Beside these lowest energy configurations, we also calculated energies of other defect configurations (local minima) where the two defects are positioned far apart. We found that the energy of a defect pair is significantly affected by the distance between the individual defects. Here we present some of the characteristic defect configurations and the corresponding energies (**Table 3**). A list of all configurations we calculated are shown in **Fig. S1**.

First, we focus on the LiCl Schottky pair. In LiCl defective systems, one Li and one Cl are removed from the corresponding sites. We observed a general trend that the closer  $V_{\text{Li}}'$  is to the  $V_{\text{Cl}}'$ , the lower defect energy is. However,

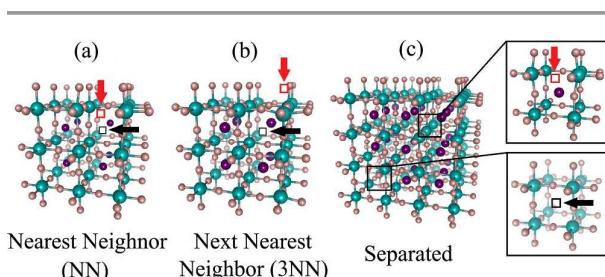


**Fig. 2** Defect configurations of the LiCl Schottky pair ( $V_{\text{Li}}' - V_{\text{Cl}}'$ ). The configurations shown in (a) Nearest Neighbor (NN), (b) Next Nearest Neighbor (3NN), and (c) Separated correspond to different relative sites of  $V_{\text{Li}}' - V_{\text{Cl}}'$ . Figures in the black boxes show the atomic arrangements near individual defects. Arrows and hollow squares are used to highlight the  $V_{\text{Cl}}'$  (black) and the  $V_{\text{Li}}'$  (red).

**Table 3** Relative energies of different  $V_{\text{Li}}^{\prime}-V_{\text{Cl}}^{\prime}$ ,  $2V_{\text{Li}}^{\prime}-V_{\text{O}}^{\bullet}$  and  $\text{Li}_i^{\prime}-\text{O}_{\text{Cl}}^{\prime}$  configurations

	Configuration	NN	3NN	4NN	Separated
LiCl Schottky	$V_{\text{Li}}^{\prime}-V_{\text{Cl}}^{\prime}$ distance /Å	2.75	4.75	6.16	8.27
	Relative energy /meV	58	0	113	101
	Configuration	Opposite	Adjacent	Separated 1	Separated 2
Li <sub>2</sub> O Schottky	$V_{\text{Li}}^{\prime}-V_{\text{O}}^{\bullet}$ distance /Å	1.94/1.94*	1.94/1.94*	5.81/1.94*	5.81/1.94*
	Relative energy /meV	0	6	697	700
	Configuration	Orientation 1	Orientation 2	Orientation 3	Separated
Li <sub>2</sub> O solution	$\text{Li}_i^{\prime}-\text{O}_{\text{Cl}}^{\prime}$ distance /Å	1.77	1.72	1.75	9.33
	Relative energy /meV	0	27	47	811

\* The two values shown in the Li<sub>2</sub>O Schottky case represent the distances between the two  $V_{\text{Li}}^{\prime}$  and the  $V_{\text{O}}^{\bullet}$

the nearest neighbour (NN) (**Fig. 2(a)**) is not the lowest energy configuration. Instead, the next nearest neighbor (3NN) configuration (**Fig. 2(b)**) has an energy 58 meV lower than that of the NN configuration. The existence of such energy minimum at the 3NN site has also been observed in other ionic conductors and has been suggested to be responsible for the high ionic conductivity.<sup>28,29</sup> We related this to the weak defect interactions as discussed in the next subsection. In order to avoid the effect of finite supercell size, we compared these results to those obtained in a 5×5×5 supercell. We obtained that even for this large supercell, the 3NN has still the lowest energy. For the case of large separation as shown in **Fig. 2(c)**, the energy is 102 meV higher than that of 3NN which is due to Coulombic interactions. This will be further discussed in the next subsection.

For the Li<sub>2</sub>O Schottky case, the oxygen vacancy ( $V_{\text{O}}^{\bullet}$ ) is surrounded by 6 lithium sites forming an octahedron. As shown in **Fig. 3(a)-(b)**, if the two  $V_{\text{Li}}^{\prime}$ 's are close to the  $V_{\text{O}}^{\bullet}$  (located on the vertices of the octahedron), then the energy is

minimized. On the other hand, as shown in **Fig. 3(c)-(d)**, if the  $V_{\text{Li}}^{\prime}-V_{\text{O}}^{\bullet}$  pair is separated, the energy is much higher (~700 meV compared with the most stable configurations). This implies a strong attraction between the  $V_{\text{Li}}^{\prime}$ 's and the  $V_{\text{O}}^{\bullet}$ .

In the lithium interstitial ( $\text{Li}_i^{\prime}$ ) case, one Cl atom is substituted by an oxygen atom to form  $\text{O}_{\text{Cl}}^{\prime}$ . The substitutional O is surrounded by 8 oxygen atoms which construct an O cube. We found that if the  $\text{Li}_i^{\prime}$  is initially close to the  $\text{O}_{\text{Cl}}^{\prime}$ , it will eventually fall into the O cube (after energy minimization) and form a dimer with the substitutional O. We also found that the orientation of the O-Li dimer is sensitive to the initial  $\text{Li}_i^{\prime}$  position. We obtained 3 different configurations in total, corresponding to 3 different orientations of the O-Li dimer. The most stable one is shown in **Fig. 4(a)**, where the O-Li dimer points to one of the O cube vertices. The other two (**Fig. 4(b)-(c)**) have slightly higher energies where the dimers orient towards the middle point of the cube edge and the center of the cube face, respectively. These configurations are different from the Li-Li dumbbell as described elsewhere<sup>19,21</sup> and the

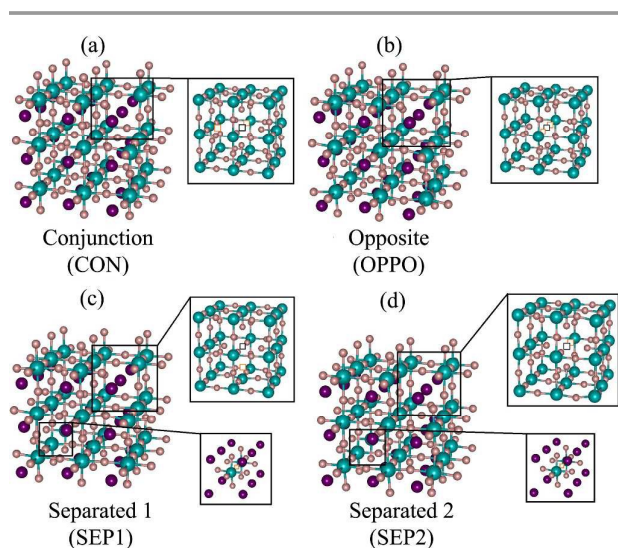


**Fig. 3** Defect configurations of the Li<sub>2</sub>O Schottky pair ( $V_{\text{Li}}^{\prime}-V_{\text{O}}^{\bullet}$ ). In (a) and (b), the two  $V_{\text{Li}}^{\prime}$ 's are on the adjacent and opposite vertices of the  $V_{\text{O}}^{\bullet}$  octahedron. In (c) and (d) the  $V_{\text{Li}}^{\prime}$ 's are separated from the  $V_{\text{O}}^{\bullet}$ . Figures in the black boxes show the atomic arrangements near individual defects. Arrows and hollow squares are used to highlight the  $V_{\text{O}}^{\bullet}$  (black) and the  $V_{\text{Li}}^{\prime}$  (red).

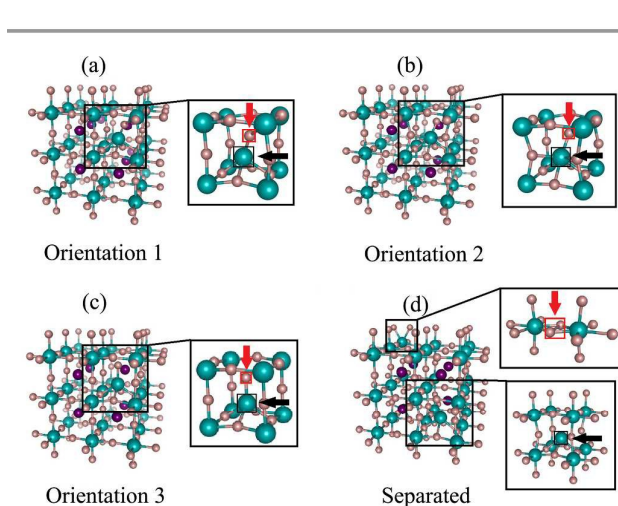


**Fig. 4** Defect configurations of the Li interstitial with a substitutional O on the Cl site ( $\text{Li}_i^{\prime}-\text{O}_{\text{Cl}}^{\prime}$ ). (a), (b) and (c) show three different orientations of the Li-O dimer. (d) shows the situation where  $\text{Li}_i^{\prime}$  and  $\text{O}_{\text{Cl}}^{\prime}$  are separated apart. Figures in the black boxes zoom into the atomic arrangements near individual defects. Arrows and hollow squares are used to highlight the  $\text{O}_{\text{Cl}}^{\prime}$  (black) and the  $\text{Li}_i^{\prime}$  (red).

**Table 4** Migration barrier, binding energy and estimated activation energy from DFT calculations

Charged defect (defect counterpart, chemical formula)	Migration barrier/ meV	Binding energy/ meV	Activation energy/ meV	Low energy pathway/ meV
$\text{Li}_i^+(\text{O}_{\text{Cl}}^-, \text{Li}_{3-x}\text{O}_{1-x}\text{Cl}_{1-x})$	147 <sup>19</sup>	642	789	-
$\text{V}_{\text{Li}}^+(\text{V}_{\text{O}}^{2+}, \text{Li}_{3-x}\text{O}_{1-0.5x}\text{Cl})$	310 <sup>18</sup>	736	1046	-
$\text{V}_{\text{Li}}^+(\text{V}_{\text{Cl}}^-, \text{Li}_{3-x}\text{OCl}_{1-x})$	310 <sup>18</sup>	145	455	<340

formation of such O-Li dimer is likely due to the strong defect Coulombic interaction as discussed in the next subsection. If the  $\text{Li}_i^+$  and the  $\text{O}_{\text{Cl}}^-$  are separated, the dimer no longer exists and the  $\text{Li}_i^+$  inserts into the lattice forming a Li-Li dumbbell (**Fig. 3(d)**). Similar to previous two cases, this separation of the two individual defects leads to higher energy (811 meV compared with the most stable one).

**Defect interactions.** The above configuration calculations indicate an attractive interaction of the defect pairs. We quantified these interactions by calculating their binding energies. Additionally, we performed Bader charge analysis,<sup>30</sup> electron localization function (ELF) analysis,<sup>31,32</sup> and covalency metric analysis<sup>33-35</sup> to reveal the nature of bonds in  $\text{Li}_3\text{OCl}$  and the origin of different defect interactions.

As shown in **Table 4**, the binding energy of  $\text{Li}_i^+$  and  $\text{O}_{\text{Cl}}^-$  is 642 meV. This large positive value indicates that the defects in this pair tend to have a strong attraction, implying  $\text{O}_{\text{Cl}}^-$  could localize the motion of  $\text{Li}_i^+$ . Similar strong attractive defect interaction is also found between  $\text{V}_{\text{Li}}^+$  and  $\text{V}_{\text{O}}^{2+}$  with a binding energy of 736 meV, resulting in a strong localization of  $\text{V}_{\text{Li}}^+$ . In the  $\text{V}_{\text{Li}}^+-\text{V}_{\text{Cl}}^-$  case, although  $\text{V}_{\text{Li}}^+$  also bonds with  $\text{V}_{\text{Cl}}^-$ , the binding energy is much smaller (145 meV). Hence, the attraction between these two defects is less significant.

To elucidate the origin of the difference among the interaction energies computed for  $\text{V}_{\text{Li}}^+-\text{V}_{\text{Cl}}^-$ ,  $\text{V}_{\text{Li}}^+-\text{V}_{\text{O}}^{2+}$ , and  $\text{O}_{\text{Cl}}^- - \text{Li}_i^+$ , we carried out Bader charge analysis and ELF analysis. As shown in **Fig. 5(a)** (pristine material), the atoms are all separated by a low electron density region and the electrons are localized around the nucleus. This indicates that the bonds in  $\text{Li}_3\text{OCl}$  are highly ionic, which is also supported by Bader charge analysis and ELF analysis. The atomic Bader charges of Li, O, and Cl are +0.88, -1.70, and -0.94, close to their formal

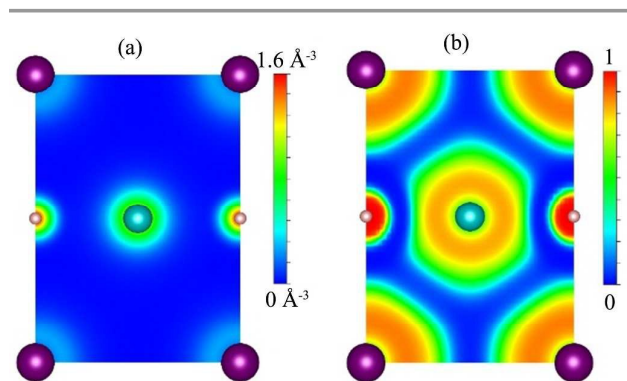


**Fig. 5** (a) A (1 1 0) plane slice of the valence electron density of defect free  $\text{Li}_3\text{OCl}$  (b) A (1 1 0) plane slice of the ELF of defect free  $\text{Li}_3\text{OCl}$ .

charges. In addition, as shown in **Fig. 5(b)**, the ELF values between the cores are low, meaning the covalent nature of bonds is weak.<sup>31,32</sup>

In defective systems, electron density, ELF, and Bader charge analysis results are virtually identical to those computed for the pristine systems. This implies that the defect interactions are mainly Coulombic so the binding energies could be obtained from the charges and the distances of the defect pairs. The weak interaction between the  $\text{V}_{\text{Li}}^+$  and the  $\text{V}_{\text{Cl}}^-$  is likely linked to the relatively large distance (3NN configuration) and the low defect charge states. The strong binding between  $\text{V}_{\text{Li}}^+$  and  $\text{V}_{\text{O}}^{2+}$ , on the other hand, results from the high +2 charge state of the O vacancy and the small distance of the defect pair (NN configuration).

For the  $\text{O}_{\text{Cl}}^- - \text{Li}_i^+$  case, although the charges of individual defects are low, the defect attraction is strong. We attribute this strong interaction to the more covalent nature of the Li-O bond in the Li-O dimer compared with the bonds in perfect lattice. To support our argument, we calculated the covalency metric proposed by Cammarata *et al.*<sup>33-35</sup> For O-Li bonds in perfect crystals, we obtained a covalency metric of -2.25 eV and for the O-Li bond in the O-Li dimer, the value is -2.18 eV. The latter larger value indicates that the O-Li bond in O-Li

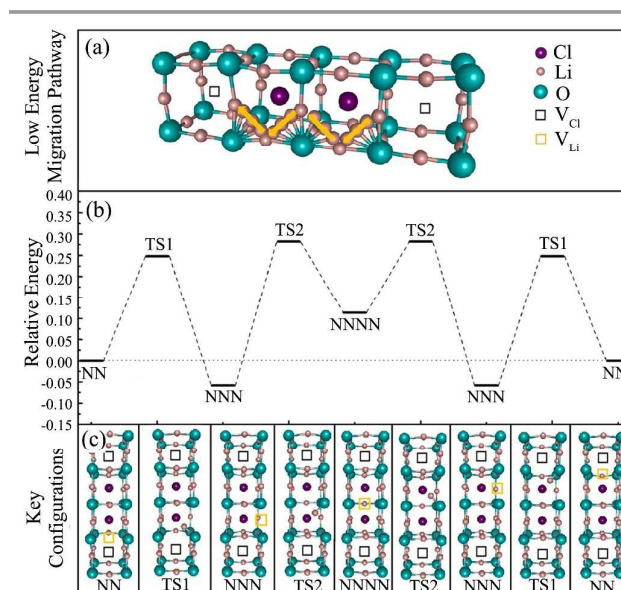


**Fig. 6** Typical low energy lithium pathway between two adjacent  $\text{V}_{\text{Cl}}^-$ 's calculated in a periodic  $3 \times 3 \times 3$  supercell (with only part of the supercell shown to make the view clearer) and the energy landscape of a lithium migrating through the low energy pathway. NN, 3NN, 4NN ( $n^{\text{th}}$  nearest neighbor) correspond to the  $\text{V}_{\text{Li}}^+$  position with respect to the  $\text{V}_{\text{Cl}}^-$ . TS1 (Transitional State 1) and TS2 (Transitional State 2) are the transition states during the hopping events.

dimer is more covalent compared with O-Li bonds in perfect lattice. This higher covalent nature, we believe, might be the cause of the strong defect interaction in  $O'_{Cl}-Li'_i$ . During the evaluations of covalency metrics, we chose the 2s and 2p orbitals of Li and O, respectively. Detailed derivation and computation methods could be found in the original work by Cammarata *et al.*<sup>33-35</sup>

**Low energy migration pathways.** As discussed in Section 3.1, the extent of defect interactions vary within a broad range (with binding energies from  $\sim 100$  meV to  $\sim 700$  meV). In order to quantify the effect of these defect interactions on Li ion diffusion, we followed the work of Wei *et al.*<sup>36</sup> and estimated the activation energy ( $E_{\text{activation}}$ ) of Li ion diffusion as the sum of the migration barrier of the charge carrier in absence of the charge compensating defects and the binding energy

$$E_{\text{activation}} = E_{\text{barrier}} + E_{\text{binding}} \quad (4)$$

where  $E_{\text{barrier}}$  and  $E_{\text{binding}}$  are the lithium migration barrier and defect binding energy respectively.

The estimated activation energies based on (4) are shown in **Table 4**. Although Li interstitials have a lower migration barrier  $E_{\text{barrier}}$  in comparison to lithium vacancies,<sup>19</sup> the overall activation energy is higher due to the strong defect interaction. Particularly in LiCl Schottky systems, the binding energy is much smaller than the other two (by  $\sim 500$  meV). This leads to the lowest activation energy among the considered defect types indicating LiCl Schottky is the most energetically favorable one for Li ion diffusion. We note that these activation energies are significantly larger than those observed in both the experimental<sup>15</sup> and the MD simulations (Section 3.2). This is because (4) corresponds to the situations where the defects are dilute and the interactions between  $O'_{Cl}$  and  $O'_{Cl}$  (or  $V_{Cl}^* - V_{Cl}^*$  and  $V_{O}^{**} - V_{O}^{**}$ ) can be ignored. However, as suggested by Zhao *et al.*<sup>15</sup> the high conductivity and low activation energy that was experimentally observed could originate from a depletion of Li and Cl ions leading to a high  $V_{Li} - V_{Cl}^*$  defect concentration. Thus, it is necessary to account for the situation where the  $O'_{Cl}-O'_{Cl}$  (or  $V_{Cl}^*-V_{Cl}^*$  and  $V_{O}^{**}-V_{O}^{**}$ ) distances are small. Here, by identifying low energy migration

**Table 5.** The energy barrier of lithium migration calculated using the FF-NEB method and a comparison with published DFT-NEB results

Migration barrier	FF-NEB	DFT-NEB
Vacancy mediated	308 meV	310-367 meV <sup>18,19</sup>
Interstitial mediated	139 meV	145 meV <sup>19</sup>

pathways between two nearby  $V_{Cl}^*$  we illustrate that the overall energy barrier could be lower than estimated from (4). One possible low energy pathway between two nearby Cl vacancies is shown in **Fig. 6** (the detailed calculation scheme and several other pathways are shown in the Supplementary Information). The corresponding activation energy is  $\sim 340$  meV. This is smaller than the 455 meV calculated using (4) and suggests that lithium ions could migrate through low energy pathways between  $V_{Cl}^*$  pairs instead of dissociating from them first. The formation of these low energy pathways may contribute to the experimentally observed high conductivity and low activation energy.

The above discussions is only qualitative and an exhaustive enumeration of all possible pathways is impractical so the evaluation of diffusion properties cannot be based on this descriptor. Therefore, in order to calculate the Li diffusion coefficient with different defect concentrations, we used classical MD simulations as discussed in the next section.

### 3.2 MD simulations and lithium transport

**Benchmarking the forced-field parameters.** Force-field based MD simulations were carried out to elucidate the diffusion properties in different systems with different defect concentrations. We benchmarked a number of properties (i.e. lattice parameters, thermal expansion coefficients, lithium migration barriers, and self-diffusivities) against experimental and DFT results. We first computed the lattice parameters of  $Li_3OCl$  based on short NPT runs. As shown in **Fig. 7 (a)**, at 300K, the lattice parameter of this work is 3.902 Å, in reasonable agreement with the published DFT (3.907 Å<sup>18</sup>) and experimental data (3.84 Å<sup>15</sup>). The linear thermal expansion coefficient is  $2.05 \times 10^{-5}$  and the published ones are  $1.8 \times 10^{-5}$  and  $2.05 \times 10^{-5}$ .<sup>15,18</sup> We then computed the migration barriers using force-field NEB (FF-NEB) calculations. **Fig. 7 (b)** shows the

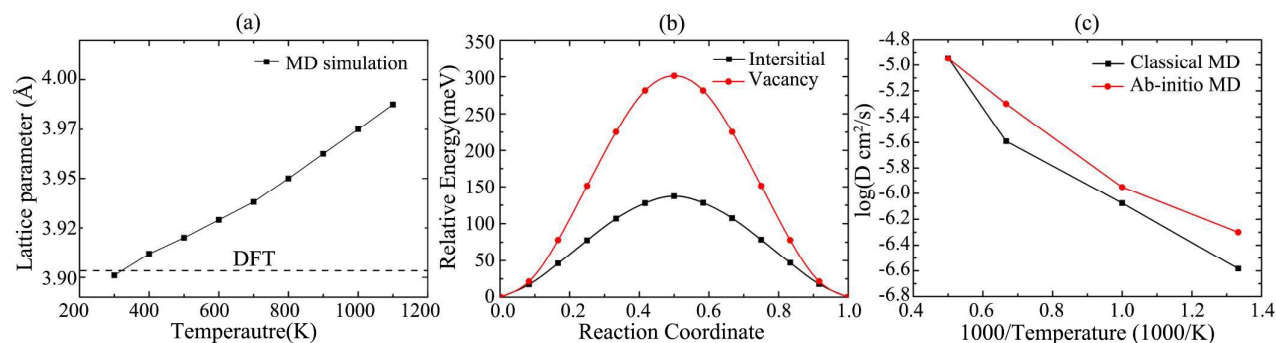


**Fig. 7** (a) Lattice parameter of  $Li_3OCl$  obtained using classical MD simulations and DFT calculations; (b) the energy landscape of the lithium migration process based on force-field NEB calculations (c) comparison of the lithium self-diffusion coefficients based on classical MD (our work) and *ab initio* MD simulations<sup>18</sup> (published) using the same  $2 \times 2 \times 2$  supercell containing one lithium vacancy.

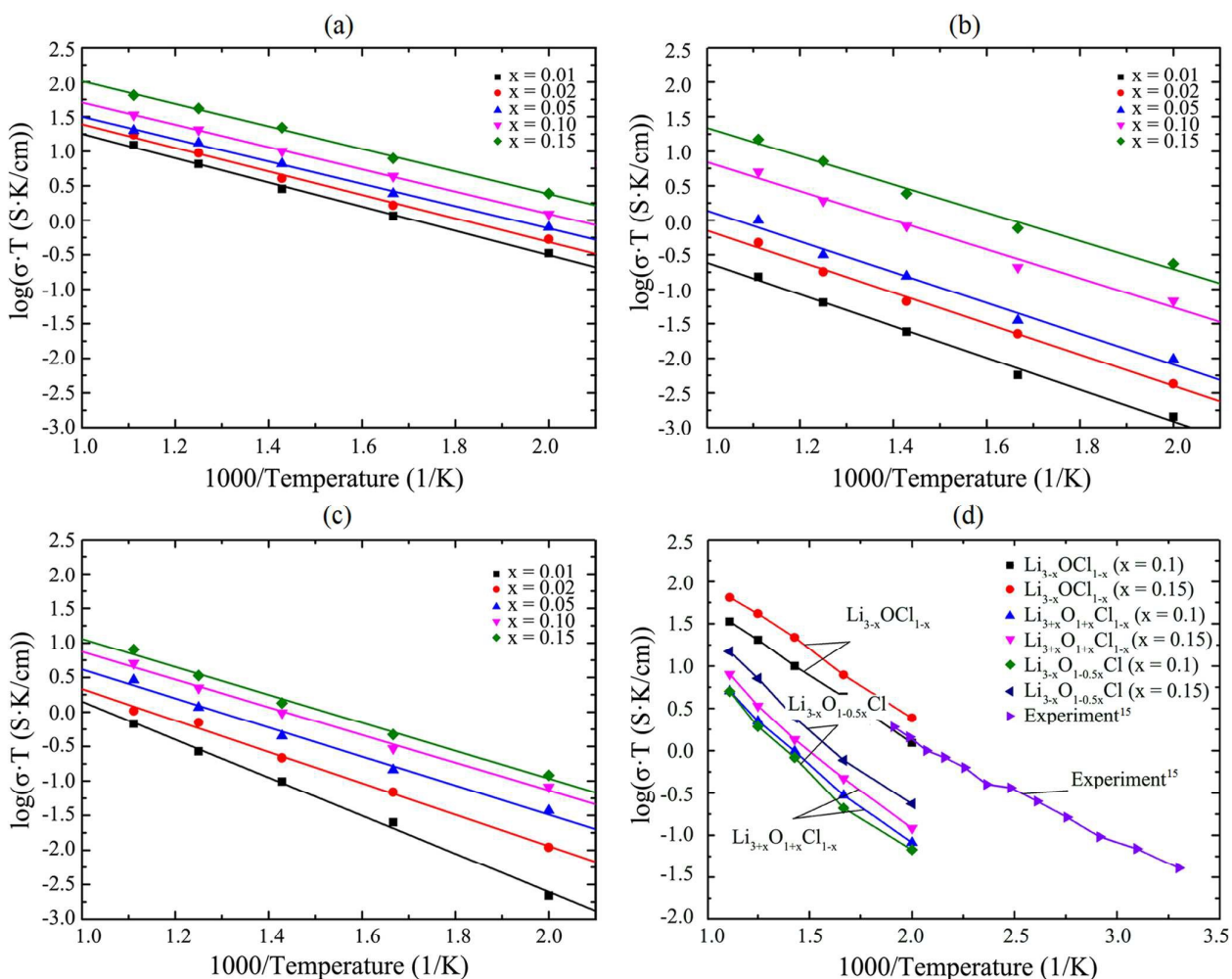


**Fig. 8** Logarithm of the lithium conductivity multiplied by the temperature in (a)  $\text{Li}_{3-x}\text{OCl}_{1-x}$  (b)  $\text{Li}_{3-x}\text{O}_{1-0.5x}\text{Cl}$  (c)  $\text{Li}_{1+x}\text{O}_{1+x}\text{Cl}_{1-x}$  as computed by MD simulations and (d) compared to experimental values.

energy of each image of FF-NEB calculations. The reaction coordinate corresponds to the normalized distance between the initial and final images of the hopping sites. Comparisons of migration barriers of the lithium interstitial and lithium vacancy with reported values<sup>18, 19</sup> are shown in **Table 5**. Our values based on FF-NEB calculations are in a good agreement with those obtained using DFT. Finally, direct comparisons of self-diffusivities based on Classical MD and published *ab initio* MD<sup>18</sup> are shown in **Fig. 7 (c)**. These values are consistent.

**Lithium transport.** We evaluated the Li ion diffusion properties by calculating the self-diffusion coefficient of lithium ions in LiCl deficient,  $\text{Li}_2\text{O}$  deficient and Li excess

systems based on MD trajectories. These coefficients were computed by fitting the mean squared displacements.<sup>37</sup> We also calculated ionic conductivities based on the Nernst-Einstein relation.<sup>38</sup> The thermodynamic factor in this work was taken to be 1. Due to the deviation from the dilute limit, this assumption could lead to an overestimation of the calculated ionic conductivities compared with the experimentally measured chemical diffusivities.<sup>22, 27</sup> However, since main goal of this work is to explore the defect chemistry impact on diffusion properties in LiRAP rather than compare the absolute values, this thermodynamic correction is not taken.

As is shown in **Fig. 8**, the LiCl Schottky defect leads to the

**Table 6** Activation energies of lithium ion diffusion in Li vacant and Li interstitial systems

Models/ $E_a$ (meV)	$x = 0.01$	$x = 0.02$	$x = 0.05$	$x = 0.10$	$x = 0.15$	Experiment
$\text{Li}_{3-x}\text{OCl}_{1-x}$ (Vac.)	347	337	320	320	312	
$\text{Li}_{3-x}\text{O}_{1-0.5x}\text{Cl}$ (Vac.)	455	442	445	416	405	$\sim 300^{15}$
$\text{Li}_{3+x}\text{O}_{1+x}\text{Cl}_{1-x}$ (Int.)	545	450	416	397	401	

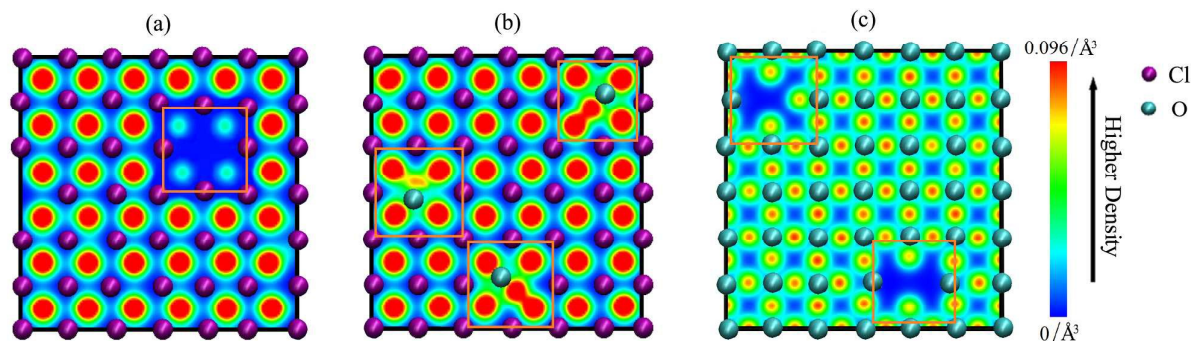


**Fig. 9** Lithium nuclear density in (a) Li-Cl plane in  $\text{Li}_{3-x}\text{OCl}_{1+x}$ , (b) Li-Cl plane in  $\text{Li}_{3-x}\text{O}_{1-x}\text{Cl}_{1+x}$  and (c) Li-O plane in  $\text{Li}_{3-x}\text{O}_{1-0.5x}\text{Cl}$  (600K,  $x = 0.10$ ). The densities were computed by binning the Li positions and averaging over 5000 snapshots sampled from the 2 ns NVT runs. Defective areas are highlighted using orange squares.

highest ionic conductivity while the other two defects are characterized by much lower Li ion diffusivities (by one order of magnitude). Also, as listed in **Table 6**, the activation energies of lithium ion diffusion in LiCl deficient systems are  $\sim 300$  meV. These values are in good agreement with the experimentally measured activation energies (200-320 meV)<sup>15</sup> while the other two computed activation energies are higher ( $>400$  meV). These results support our argument that a LiCl deficient environment favors Li ion diffusion. We also note that the activation energies decrease with increasing LiCl Schottky concentrations. This is probably due to the presence of low energy pathways in highly defective systems as discussed in Section 3.1.

The above MD based activation energy results agree with the DFT-based binding energies evaluation, where a weak defect interaction was obtained between  $V_{\text{Cl}}^*$  and  $V_{\text{Cl}}^*$ . However, as reported in previous theoretical work,<sup>19,21</sup> another contribution to Li ion diffusivity should also be considered, i.e., the intrinsic migration barriers of charge carriers. It was suggested that Li interstitials have lower migration barriers than the Li vacancies.<sup>19</sup> Since both the defect binding and the intrinsic migration barrier effects on Li diffusion are included in MD simulations,<sup>19,21</sup> the higher diffusivities of Li vacancies in LiCl cases suggest that the defect interactions have as strong effects on diffusion as the intrinsic migration barrier.

It is important to note that some of the simulations were undertaken beyond the operating temperature range of  $\text{Li}_3\text{OCl}$  solid electrolyte and no core-shell model was adopted in the present study. However, as shown in the previous subsection, the classical MD simulation results have been benchmarked against experimental data and DFT calculations in terms of lattice parameters, migration barriers and diffusion coefficients.

**Lithium ion trajectories and characteristic hopping events.** The DFT-based energy calculations discussed above show a general trend that both  $V_{\text{Li}}^*$ 's and  $\text{Li}_i^*$ 's have lower energies when bound to their paired defects. To give a direct visualization of these attractive defect interactions, we show the nuclear density map of lithium atoms based on MD trajectories in **Fig. 9**. The nuclear density of lithium ions in the Li-Cl plane and Li-O plane is shown in **Fig. 9(a)-(b)** and

**Fig. 9(c)**, respectively. The lithium density near  $V_{\text{Cl}}^*$ 's (**Fig. 9(a)**) and  $V_{\text{O}}^{**}$ 's (**Fig. 9(c)**) is lower than the region with no  $V_{\text{Cl}}^*/V_{\text{O}}^{**}$ 's. This implies a higher probability of a  $V_{\text{Li}}^*$  existing around its corresponding paired defect, i.e.,  $V_{\text{Cl}}^*$  or  $V_{\text{O}}^{**}$ . This is in agreement with the previously discussed attraction between the  $V_{\text{Li}}^*$  and the  $V_{\text{Cl}}^*/V_{\text{O}}^{**}$ . Similar attractive interactions are also found in Li excess systems where  $\text{Li}_i^*$ 's are tightly confined around the  $\text{O}'_{\text{Cl}}$ . As shown in **Fig. 9(b)**, the previously discussed O-Li dimer is directly visualized where the nuclear density of lithium is high around the  $\text{O}'_{\text{Cl}}$ . The semicircle region of lithium ions around the  $\text{O}'_{\text{Cl}}$  corresponds to rotation of the O-Li dimer (within a small angle). One typical rotation is drawn in **Fig. 10(a)**.

To complete our discussion, we also noted that in **Fig. 9(a)-(b)**, the high lithium density regions are disjoint. This means that the diffusion of lithium ions in the Li-Cl plane is not significant. In contrast, the non-zero lithium density regions are connected in the Li-O plane, indicating a higher probability of lithium ions channeling along the edges of an oxygen octahedron. This is in agreement with previously published work in which a low migration barrier along the edge of the octahedron is reported.<sup>21</sup> One typical hopping event of Li to adjacent vacant site along the oxygen octahedral edge is shown in **Fig. 10(b)**.

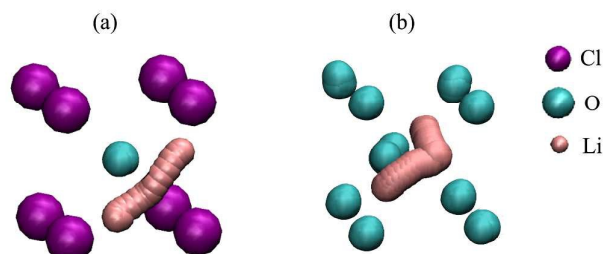


**Fig. 10** (a) Characteristic lithium-oxygen dimer rotation in  $\text{Li}_{3-x}\text{O}_{1-x}\text{Cl}_{1+x}$ . (b) Characteristic lithium hopping towards adjacent lithium vacancy in  $\text{Li}_{3-x}\text{OCl}_{1-x}$  and  $\text{Li}_{3-x}\text{O}_{1-0.5x}\text{Cl}$ . In order to make hopping events clearer, only the related lithium atoms in both (a) and (b) are shown. Cl atoms in (a) are not shown.

#### 4. Conclusions

We conducted first-principle DFT calculations and classical MD simulations to study the defect chemistry and the lithium ion migration in  $\text{Li}_3\text{OCl}$ , a prototypical LiRAP. Three types of charge neutral defect pairs, namely  $\text{O}'_{\text{Cl}}-\text{Li}^*_i$ ,  $\text{V}'_{\text{Li}}-\text{V}^*_{\text{Cl}}$  and  $2\text{V}'_{\text{Li}}-\text{V}^*_{\text{O}}$  were investigated. We found that while the three types of defect pairs have similar formation energies, they lead to different Li ion diffusivities.  $\text{V}'_{\text{Li}}-\text{V}^*_{\text{Cl}}$  is the most energetically favorable for fast Li ion diffusion because its binding energy is significantly lower than the other two. Classical MD simulations also show that the  $\text{Li}_{3-x}\text{OCl}_{1-x}$  systems have high ionic conductivity and the computed activation energies are comparable to reported experimental values. Our results support the formation of LiCl Schottky defects and a Li vacancy hopping mechanism. Hopefully, the current study will not only lead to better understanding of diffusion process in LiRAP, but it will also benefit experimentalists by providing a way to computationally screen the defect types so as to enhance ionic conductivity in highly ordered configurations like  $\text{Li}_3\text{OCl}$ .

#### Acknowledgements

The authors gratefully acknowledge the Research Grants Council of Hong Kong for support through the projects DAG12EG06 and ECS 639713. Zarah Medina Baiyee acknowledges the support of the Hong Kong PhD Fellowship Scheme.

#### References

1. V. Etacheri, R. Marom, R. Elazari, G. Salitra and D. Aurbach, *Energy Environ. Sci.*, 2011, **4**, 3243-3262.
2. Y. Wang, B. Liu, Q. Li, S. Cartmell, S. Ferrara, Z. D. Deng and J. Xiao, *J. Power Sources*, 2015, **286**, 330-345.
3. M. M. Thackeray, C. Wolverton and E. D. Isaacs, *Energy Environ. Sci.*, 2012, **5**, 7854-7863.
4. B. Scrosati, J. Hassoun and Y.-K. Sun, *Energy Environ. Sci.*, 2011, **4**, 3287-3295.
5. C. M. Hayner, X. Zhao and H. H. Kung, *Annu. Rev. Chem. Biomol. Eng.*, 2012, **3**, 445-471.
6. L. Lu, X. Han, J. Li, J. Hua and M. Ouyang, *J. Power Sources*, 2013, **226**, 272-288.
7. J. G. Kim, B. Son, S. Mukherjee, N. Schuppert, A. Bates, O. Kwon, M. J. Choi, H. Y. Chung and S. Park, *J. Power Sources*, 2015, **282**, 299-322.
8. E. Quartarone and P. Mustarelli, *Chem. Soc. Rev.*, 2011, **40**, 2525-2540.
9. G. F. Ortiz, M. C. López, P. Lavela, C. Vidal-Abarca and J. L. Tirado, *Solid State Ionics*, 2014, **262**, 573-577.
10. K. Arbi, W. Bucheli, R. Jiménez and J. Sanz, *J. Eur. Ceram. Soc.*, 2015, **35**, 1477-1484.
11. V. Thangadurai, S. Narayanan and D. Pinzar, *Chem. Soc. Rev.*, 2014, **43**, 4714-4727.
12. R. Murugan, V. Thangadurai and W. Weppner, *Angew. Chem. Int. Ed.*, 2007, **46**, 7778-7781.
13. Y. Seino, T. Ota, K. Takada, A. Hayashi and M. Tatsumisago, *Energy Environ. Sci.*, 2014, **7**, 627-631.
14. F. Mizuno, A. Hayashi, K. Tadanaga and M. Tatsumisago, *Solid State Ionics*, 2006, **177**, 2721-2725.
15. Y. Zhao and L. L. Daemen, *J. Am. Chem. Soc.*, 2012, **134**, 15042-15047.
16. N. Kamaya, K. Homma, Y. Yamakawa, M. Hirayama, R. Kanno, M. Yonemura, T. Kamiyama, Y. Kato, S. Hama and K. Kawamoto, *Nat. Mater.*, 2011, **10**, 682-686.
17. M. Braga, J. A. Ferreira, V. Stockhausen, J. Oliveira and A. El-Azab, *J. Mater. Chem. A*, 2014, **2**, 5470-5480.
18. Y. Zhang, Y. Zhao and C. Chen, *Phys. Rev. B: Condens. Matter*, 2013, **87**, 134303.
19. A. Emly, E. Kioupakis and A. Van der Ven, *Chem. Mater.*, 2013, **25**, 4663-4670.
20. M.-H. Chen, A. Emly and A. Van der Ven, *Phys. Rev. B: Condens. Matter*, 2015, **91**, 214306.
21. R. Mouta, M. A. B. Melo, E. M. Diniz and C. W. A. Paschoal, *Chem. Mater.*, 2014, **26**, 7137-7144.
22. Z. Deng, B. Radhakrishnan and S. P. Ong, *Chem. Mater.*, 2015.
23. G. Kresse and J. Furthmüller, *Phys. Rev. B: Condens. Matter*, 1996, **54**, 169.
24. P. E. Blöchl, *Phys. Rev. B: Condens. Matter*, 1994, **50**, 17953.
25. M. Nakayama and M. Martin, *Phys. Chem. Chem. Phys.*, 2009, **11**, 3241-3249.
26. S. Plimpton, P. Crozier and A. Thompson, *Sandia National Laboratories*, 2007, **18**.
27. R. Gomer, *Rep. Prog. Phys.*, 1990, **53**, 917-1002.
28. B. Wang, X. Xi and A. N. Cormack, *Chem. Mater.*, 2014, **26**, 3687-3692.
29. B. Wang, R. J. Lewis and A. N. Cormack, *Acta Mater.*, 2011, **59**, 2035-2045.
30. R. F. Bader, *Atoms in molecules*, Wiley Online Library 1990.
31. A. D. Becke and K. E. Edgecombe, *J. Chem. Phys.*, 1990, **92**, 5397-5403.
32. A. Savin, R. Nesper, S. Wengert and T. F. Fässler, *Angew. Chem. Int. Ed. in English*, 1997, **36**, 1808-1832.

## ARTICLE

Journal Name

33. A. Cammarata and T. s. Polcar, *Inorg. Chem.*, 2015, **54**, 5739–5744.
34. A. Cammarata and J. M. Rondinelli, *J. Chem. Phys.*, 2014, **141**, 114704.
35. A. Cammarata, W. Zhang, P. S. Halasyamani and J. M. Rondinelli, *Chem. Mater.*, 2014, **26**, 5773-5781.
36. X. Wei, W. Pan, L. Cheng and B. Li, *Solid State Ionics*, 2009, **180**, 13-17.
37. M. P. Allen and D. J. Tildesley, *Computer simulation of liquids*, Oxford University Press, 1989.
38. J. M. Bockris and A. K. Reddy, *Modern electrochemistry: an introduction to an interdisciplinary area. Vol. 1*, Plenum Press, 1970.